

# Centrifugal-sudden hyperspherical study of $\text{Cl} + \text{HCl} \rightarrow \text{ClH} + \text{Cl}$ reaction dynamics on ‘tight-bend’ and ‘loose-bend’ potential energy surfaces

D. Sokolovski<sup>a</sup>, J.N.L. Connor<sup>b,\*</sup>, G.C. Schatz<sup>c,1</sup>

<sup>a</sup> *The Theoretical and Computational Physics Research Division, The Department of Applied Mathematics and Theoretical Physics, The School of Mathematics and Physics, The Queen's University of Belfast, Belfast BT7 1NN, UK*

<sup>b</sup> *Department of Chemistry, University of Manchester, Manchester M13 9PL, UK*

<sup>c</sup> *Theoretical Chemistry Group, Chemistry Division, Argonne National Laboratory, Argonne, IL 60439, USA*

Received 11 January 1996

---

## Abstract

A centrifugal-sudden hyperspherical (CSH) quantum calculation has been carried out for the three-dimensional reaction  $\text{Cl} + \text{HCl} \rightarrow \text{ClH} + \text{Cl}$ , using the extended London–Eyring–Polanyi–Sato (LEPS) potential energy surface no. 3 of Persky and Kornweitz (PK3), which is an example of a ‘tight-bend’ surface. Quantities calculated include: state-to-state and cumulative reaction probabilities, and differential and integral cross sections. Comparison is made with CSH results from the ‘loose-bend’ LEPS surface of Bondi–Connor–Manz–Rörmelt (BCMR). Three simple models are used to understand qualitatively trends in the computed results from the PK3 and BCMR surfaces: (1) a classical hard-sphere model, which describes collisions of the reactants, (2) a  $J$  shift approximation for the reaction probabilities, where  $J$  is the total angular momentum quantum number, (3) a semi-classical optical model for the reactive differential cross sections. In addition, the angular distributions are analysed by an (asymptotic) nearside–farside (NF) theory in order to extract their physical content. The NF analysis shows that high frequency oscillations in the forward-angle scattering are an interference effect caused by a resonance.

---

## 1. Introduction

The isoergic chemical reaction  $\text{Cl} + \text{HCl} \rightarrow \text{ClH} + \text{Cl}$ , has been the subject of many experimental and theoretical investigations. It is an important example of a reaction in which a light atom is exchanged between

two heavy ones. Thermal and initial state-resolved rate coefficient measurements have been available for some time [1,2], whilst photodetachment experiments on  $\text{ClHCl}^-$  have provided strong evidence that long-lived resonances exist near the  $\text{ClHCl}$  saddle point [3].

In order to interpret this experimental data, it is necessary to use a potential energy surface, so that dynamics calculations can be performed. Much theoretical research has employed the semi-empirical extended London–Eyring–Polanyi–Sato (LEPS) potential surface introduced by Bondi et al. in 1983 [4]

---

\* Corresponding author.

<sup>1</sup> Permanent address: Department of Chemistry, Northwestern University, Evanston, IL 60208-3113, USA.

(this surface will be denoted BCMR). These authors calculated exact collinear quantum reaction probabilities and were the first to predict a spectrum of resonances for  $\text{Cl} + \text{HCl}$  [4].

There have been numerous studies of  $\text{Cl} + \text{HCl}$  reaction dynamics using the BCMR potential surface (too many to review here), so we just refer to some recent research [5], and summarise some important dynamical properties of the BCMR potential surface.

BCMR is an example of a ‘loose-bend’ potential surface, because the bending frequency at the  $\text{ClHCl}^\ddagger$  saddle point is relatively low. As a result, there is relatively free rotational motion of  $\text{HCl}$  all the way to the transition state, and as the products depart. More specifically, the approach of  $\text{Cl}$  towards  $\text{HCl}$  is governed mainly by repulsive torques [6]. Although the intermediate  $\text{ClHCl}$  species is often close to collinear, bent configurations can occur whilst the products are separating; the release of repulsive energy then leads to rotationally excited product  $\text{HCl}$ . This process is helped by rotational excitation of the reactant  $\text{HCl}$  molecule. One important mechanism that occurs is a ‘figure of eight’ motion. This is one in which the  $\text{H}$  atom of the incident rotating  $\text{HCl}$  molecule passes quickly between the approaching  $\text{Cl} \cdots \text{Cl}$  atoms, with the product  $\text{HCl}$  molecule spinning off in the opposite sense to that of the incident molecule.

In contrast to the loose-bend properties of BCMR, the LEPS potential surface no. 3 of Persky and Kornweitz (denoted PK3) [6] is an example of a ‘tight-bend’ surface, because it has a relatively high bending frequency at the saddle point. In this case, the approach of  $\text{Cl}$  towards  $\text{HCl}$  is governed mainly by strong attractive torques. These cause the reagents to reorientate to a nearly collinear configuration, which persists as the products start to separate, resulting in product molecules in low rotational states. This process is hindered by rotational excitation of the reactant  $\text{HCl}$  molecule (at least for low rotational quantum numbers) because it is then more difficult for  $\text{HCl}$  to align with  $\text{Cl}$ .

It is important to note that the BCMR and PK3 potential surfaces are essentially identical for the collinear configuration of the atoms [6]. They are defined in more detail in Section 2.

The dynamics of the  $\text{Cl} + \text{HCl}$  reaction on the BCMR and PK3 potential surfaces have been exam-

ined using quantum mechanical and quasiclassical trajectory (QCT) computations [4–29]. In particular, for BCMR, we and co-workers have applied the following quantum methods: centrifugal-sudden distorted-wave (CSDW) [7–9,13,16], centrifugal-sudden hyperspherical (CSH) [14–26] and coupled-channel hyperspherical (CCH) [23]. The CSDW method is a perturbative technique which is only valid at low total energies, whereas the CSH and CCH methods are non-perturbative and remain valid at higher total energies.

For the PK3 potential surface, we have also carried out CSDW computations [12,13,16], but the only CSH calculations have been restricted to a value of the total angular momentum quantum number  $J$  of zero (n.b. for  $J = 0$ ,  $\text{CSH} \equiv \text{CCH}$ ) [14–16].

It is not known at present whether the correct potential surface is tight or loose. It is therefore clearly desirable to perform quantum dynamical calculations for PK3 in order to characterise both limiting cases, in particular at total energies where the CSDW approximation is no longer valid. The purpose of the present paper is to fill this gap in the literature. We use the CSH method because the computational effort for higher partial waves with  $J > 0$  is about the same as that for  $J = 0$ . This is an important practical point for the calculation of differential and integral cross sections, where up to 171 partial waves must be computed. The CSH computations are described in Section 3.

We also systematically compare our PK3 results with those for BCMR. In some cases, we have carried out new CSH computations for BCMR. In order to understand trends in our results, we make use of three simple models.

(a) A classical hard-sphere model, which describes collisions of the reactants.

(b) The  $J$  shift approximation, which relates reaction probabilities for  $J > 0$  to those for  $J = 0$ . This approximation has been exploited extensively by Bowman and co-workers [30]. It was originally introduced by Takayanagi for inelastic scattering under the name ‘modified wavenumber approximation’ [31].

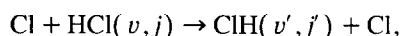
(c) A semi-classical optical model for the reactive angular distribution which relates the  $J$  dependent reaction probabilities to the reactive differential cross section. This model was introduced by Herschbach

[32]. We have used it successfully in our CSDW studies [8,10,13] (see also Ref. [11]).

An important feature of our computed results in Sections 4–6 is that they display resonance behaviour. However, the analysis of reactive resonances is more complicated than that of non-resonance scattering and is not considered in detail in this paper. Note that a general complex angular momentum (Regge pole) theory of resonance scattering has been developed by us in Refs. [25,26], and applied to  $\text{Cl} + \text{HCl}$  for the BCMR surface.

We have carried out CSH computations for PK3 and BCMR at total energies  $E$  in the range 0.30–0.70 eV, where  $E$  is measured with respect to  $\text{HCl}$  at its classical equilibrium position. At four energies, much more extensive computations have been performed. These are  $E = 0.638, 0.66, 0.68, 0.70$  eV for PK3 and  $E = 0.642, 0.66, 0.68, 0.70$  eV for BCMR; the lowest  $E$  value for each surface corresponds to the  $J = 0$  resonance energy.

CSH degeneracy-averaged integral cross sections are presented in Section 4 for the state-to-state process



where  $v$  and  $j$  are vibrational and rotational quantum numbers, respectively. We also compare the CSH cross sections summed over final states with available QCT results. Section 5 discusses the energy dependence of various state-to-state and cumulative reaction probabilities for  $J = 0$ . In Section 6, we consider the state-to-state reaction probabilities as a function of  $J$ , and the reactive differential cross sections. We have also performed an (asymptotic) nearside–farside analysis [22,33] of the angular distributions, in order to extract their physical content. Our conclusions are in Section 7.

## 2. Potential energy surfaces

The BCMR and PK3 potential surfaces are both semi-empirical extended London–Eyring–Polanyi–Sato (LEPS) surfaces. The BCMR potential [4] has identical Sato parameters of  $S(\text{HCl}) = S(\text{Cl}_2) = 0.115$ , which have been adjusted to give a classical barrier height of about 0.37 eV as recommended by Kneba and Wolfrum [2]. The PK3 surface [6] has

Table 1

Saddle point properties for the BCMR and PK3 potential energy surfaces for the  $\text{Cl} + \text{HCl} \rightarrow \text{ClH} + \text{Cl}$  reaction <sup>a</sup>

Property	Potential	
	BCMR	PK3
$R_{\text{HCl}}^\ddagger$ ( $a_0$ )	2.772	2.812
$\text{ClHCl}$ angle ( $^\circ$ )	180	180
$V^\ddagger$ (eV)	0.371	0.371
Harmonic frequencies ( $\text{cm}^{-1}$ ):		
sym. stretch	344	347
bend	508, 508	692, 692
antisym. stretch	1398i	1468i

<sup>a</sup> From Table I of Ref. [13].

Sato parameters of  $S(\text{HCl}) = 0.220$  and  $S(\text{Cl}_2) = -0.241$ .

Table 1 reports the saddle point properties of the two surfaces. For collinear geometries, BCMR and PK3 are very similar; in particular the height and position of their saddle points are almost the same. The most noticeable difference concerns their bending frequencies. This difference is large enough to make the PK3 surface significantly different in its properties from BCMR for non-collinear geometries. This has important dynamical consequences as mentioned in Section 1. For recent ab initio electronic structure calculations of the  $\text{ClHCl}$  potential surface, see Ref. [34].

## 3. Quantum dynamics calculations

The quantum scattering matrix elements were computed using a coupled-channel (CC) propagation method which employs Delves' hyperspherical (H) co-ordinates, together with a centrifugal-sudden (CS) approximation for decoupling the helicity quantum numbers. In particular, the CS approximation assumes the initial helicity quantum number of  $\Omega = 0$  is conserved throughout the reaction, so that we also have for the product quantum number,  $\Omega' = 0$ . Details of this CSH( $\Omega = 0$ ) technique have been reported in Refs. [14,19].

Note that states with  $|\Omega| > 0$  correlate adiabatically with excited bending states at the saddle point [7]. These states have higher barriers than that for  $\Omega = 0$ , and so should have smaller cross sections.

We examined this point in Ref. [23] where we compared CCH( $\Omega_{\max} = 2$ ) results with those from the CSH( $\Omega = 0$ ) approximation for the BCMR potential. Our calculations confirmed that at  $E = 0.40$

eV the dominant contribution to the scattering comes from the  $\Omega = 0$  state, although as  $E$  increases, the  $|\Omega| > 0$  states become more important.

The basis set employed for both potentials con-

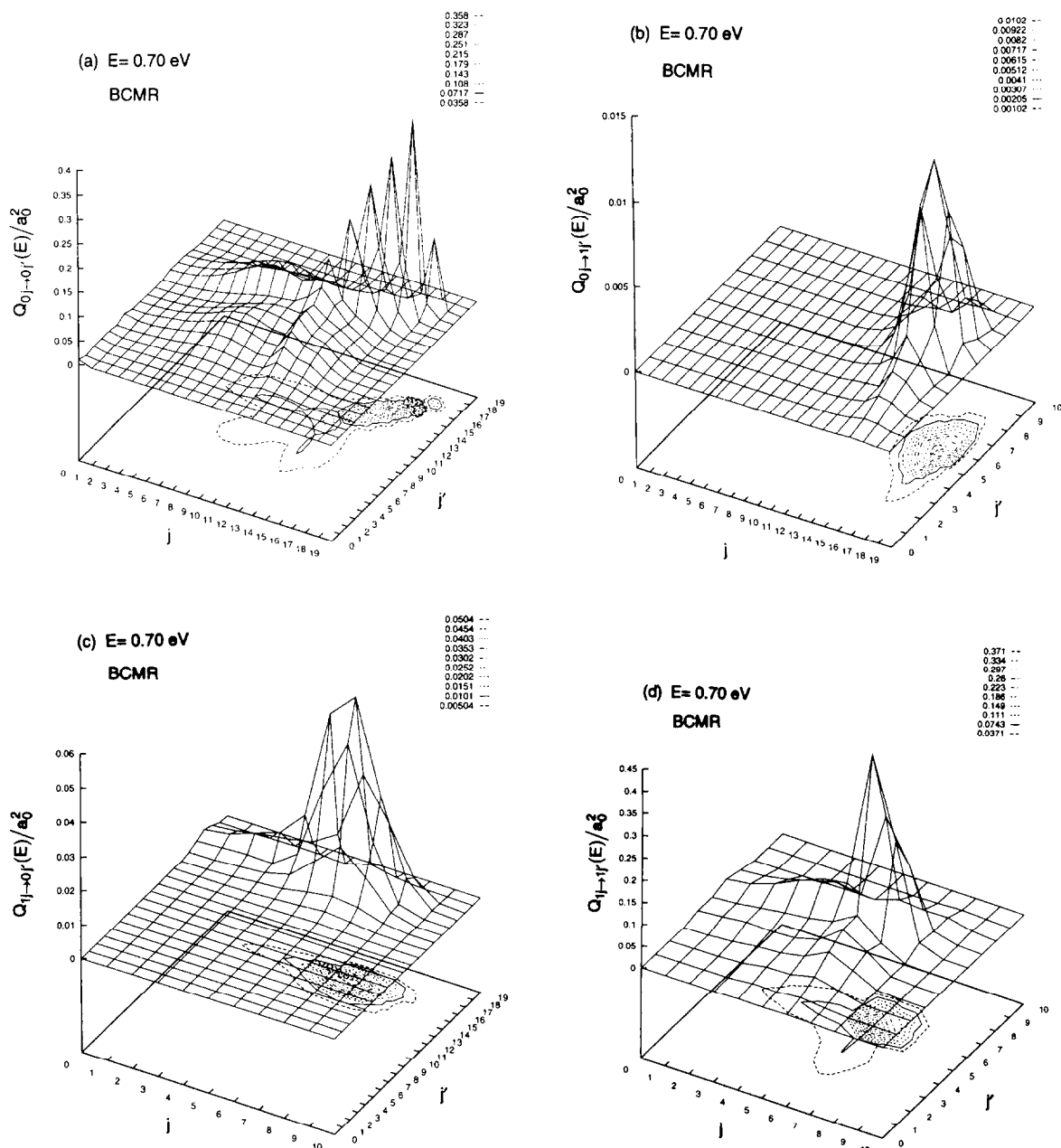


Fig. 1. Perspective and contour plots of the degeneracy averaged integral cross section  $Q_{v,j \rightarrow v',j'}(E)$  versus  $j$  and  $j'$  at  $E = 0.70$  eV for the BCMR potential surface. (a) Cross sections with  $v = 0, j \rightarrow v' = 0, j'$ , (b) cross sections with  $v = 0, j \rightarrow v' = 1, j'$ , (c) cross sections with  $v = 1, j \rightarrow v' = 0, j'$ , (d) cross sections with  $v = 1, j \rightarrow v' = 1, j'$ .

sists of 80 states, 40 for each arrangement channel. The 40 states comprise three vibrations with  $j_{\max} = 19, 13, 5$  for  $v = 0, 1, 2$ , respectively.

For the BCMR potential, we carried out  $J = 0$  calculations at  $E = 0.300$  (0.005) 0.700 eV. At four energies, namely  $E = 0.642, 0.66, 0.68, 0.70$  eV, we

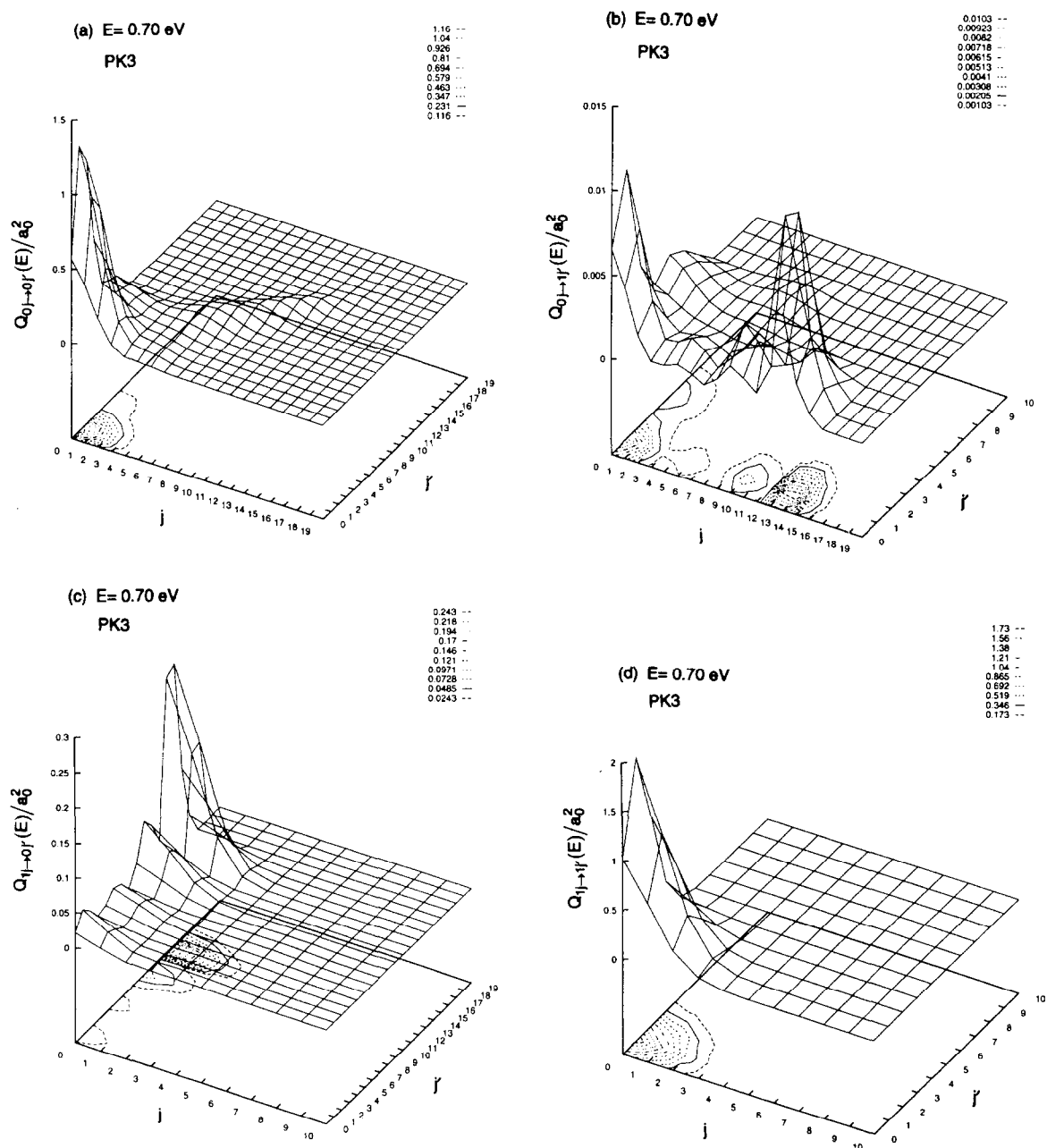


Fig. 2. Perspective and contour plots of the degeneracy averaged integral cross section  $Q_{ij \rightarrow i'j'}(E)$  versus  $j$  and  $j'$  at  $E = 0.70$  eV for the PK3 potential surface. (a) Cross sections with  $v = 0, j \rightarrow v' = 0, j'$ , (b) cross sections with  $v = 0, j \rightarrow v' = 1, j'$ , (c) cross sections with  $v = 1, j \rightarrow v' = 0, j'$ , (d) cross sections with  $v = 1, j \rightarrow v' = 1, j'$ .

computed all partial waves up to  $J_{\max} = 160$ , which is sufficient to converge partial wave sums for the differential and integral cross sections. Note that a pronounced resonance occurs at  $E = 0.642$  eV for the  $J = 0$  partial wave. Some of the results from these computations for the BCMR potential have appeared in our earlier papers [15–26].

All our results for the PK3 potential are new.  $J = 0$  calculations were performed at  $E = 0.300$  (0.005) 0.615, 0.302 (0.002) 0.618, 0.620 (0.001) 0.700 eV. All partial waves up to  $J_{\max} = 160$  were computed at  $E = 0.638$ , 0.66, 0.68 eV with  $J_{\max} = 170$  at  $E = 0.70$  eV. There is a resonance at  $E = 0.638$  eV for PK3, which is the analog of the one at  $E = 0.642$  eV for BCMR.

The primary quantity calculated by the CSH method is the state-to-state scattering matrix element at a total energy  $E$

$$S_{vj \rightarrow v'j'}^J(E),$$

together with the corresponding reaction probability

$$P_{vj \rightarrow v'j'}^J(E) = |S_{vj \rightarrow v'j'}^J(E)|^2.$$

The masses used in the calculations are  $m_{\text{H}} = 1.008$  u and  $m_{\text{Cl}} = 34.969$  u.

#### 4. Integral cross sections

The degeneracy-averaged integral state-to-state cross section  $Q_{vj \rightarrow v'j'}(E)$  is obtained from  $P_{vj \rightarrow v'j'}^J(E)$  by means of the partial wave sum

$$Q_{vj \rightarrow v'j'}(E) = \frac{1}{(2j+1)} \frac{\pi}{k_{vj}^2} \sum_{J=0}^{\infty} (2J+1) P_{vj \rightarrow v'j'}^J(E),$$

where  $k_{vj}$  is the initial translational wavenumber.

Perspective and contour plots of  $Q_{vj \rightarrow v'j'}(E)$  versus  $j$  and  $j'$  at  $E = 0.70$  eV for BCMR and PK3 are displayed in Figs. 1 and 2, respectively. Each figure comprises four plots showing cross sections with (a)  $v = 0 \rightarrow v' = 0$ , (b)  $v = 0 \rightarrow v' = 1$ , (c)  $v = 1 \rightarrow v' = 0$ , (d)  $v = 1 \rightarrow v' = 1$ . The cross sections for  $v = 0, j \rightarrow v' = 1, j'$  are related to those for  $v = 1, j \rightarrow v' = 0, j'$  by microscopic reversibility:

$$k_{vj}^2(2j+1)Q_{vj \rightarrow v'j'}(E) = k_{v'j'}^2(2j'+1)Q_{v'j' \rightarrow vj}(E). \quad (4.1)$$

Table 2

Degeneracy averaged integral cross sections  $Q_{vj \rightarrow v'j'}(E)$  at  $E = 0.70$  eV for the BCMR potential energy surface. The five largest cross sections with  $v = 0$  and the four largest cross sections with  $v = 1$  are reported. Also listed are the corresponding rovibrational eigenvalues  $E_{vj}$  of the isolated HCl molecule

Label	$v$	$j$	$E_{vj}$ (eV)	$v'$	$j'$	$E_{v'j'}$ (eV)	$Q_{vj \rightarrow v'j'}$ ( $\text{\AA}^2$ )
a	0	16	0.530	0	16	0.530	0.394
b	0	15	0.490	0	15	0.490	0.323
c	0	14	0.452	0	14	0.452	0.274
d	0	13	0.416	0	13	0.416	0.210
e	0	17	0.573	0	17	0.573	0.144
f	1	6	0.590	1	6	0.590	0.408
g	1	6	0.590	1	7	0.607	0.239
h	1	7	0.607	1	6	0.590	0.232
i	1	7	0.607	1	7	0.607	0.146

This relation is discussed in more detail below in connection with Table 2.

Firstly, we consider cross sections with  $v = 0 \rightarrow v' = 0$ . Fig. 1(a) for BCMR shows that the most reactive rotational states have  $j = 13$ –17 with  $j'$  in the same range. In contrast, Fig. 2(a) for PK3 reveals that the most reactive rotational states have  $j, j'$  lying between 0 and 2.

This same kind of behaviour applies to the  $v = 1 \rightarrow v' = 1$  case displayed in Fig. 1(d) and Fig. 2(d). On BCMR, the largest cross sections have  $j, j'$  values of 6, 7, whereas on PK3, the corresponding rotational quantum numbers are 0–2. Note that the largest cross sections on PK3 with  $v = 0 \rightarrow v' = 0$  and  $v = 1 \rightarrow v' = 1$  have comparable magnitudes. This is also true for BCMR.

Fig. 1(b) and Fig. 1(c) and Fig. 2(b) and Fig. 2(c) show that cross sections involving a change in vibrational quantum number are generally considerably smaller than the vibrationally diagonal cross sections. On BCMR, the largest vibrationally inelastic cross sections have  $v = 0, j = 16 \rightarrow v' = 1, j' = 6$  and  $v = 1, j = 6 \rightarrow v' = 0, j' = 16$ . On PK3, the corresponding cross sections have  $v = 0, j = 13 \rightarrow v' = 1, j' = 1$  and  $v = 1, j = 0 \rightarrow v' = 0, j' = 13$ . Note the high  $j, j'$  values for PK3, compared to the low values when  $v = v'$ .

The state-to-state cross sections shown in Figs. 1 and 2 are for  $E = 0.70$  eV. However similar plots are obtained at nearby values of  $E$  for which we have

made detailed calculations, namely 0.638, 0.66, 0.68 eV for PK3 and 0.642, 0.66, 0.68 eV for BCMR. In particular, the resonance has only a small effect on the distributions, as noted earlier in calculations for BCMR (which included the non-resonance energy  $E = 0.62$  eV) [19,21,24].

Table 2 lists for BCMR at  $E = 0.70$  eV the five largest cross sections  $Q_{vj \rightarrow v'j'}(E)$  having  $v = 0$  and the four largest cross sections with  $v = 1$ . Table 3 reports the corresponding cross sections for PK3. Also listed are the associated rovibrational channel energies  $E_{vj}$  and  $E_{v'j'}$  measured with respect to the minimum of the HCl potential energy curve. The transitions given in Tables 2 and 3 are studied in more detail in Sections 5 and 6.

The cross sections for the transitions  $v = 1, j = 6 \rightarrow v' = 1, j' = 7$  and  $v = 1, j = 7 \rightarrow v' = 1, j' = 6$  in Table 2 should satisfy the microscopic reversibility relation (4.1). In practice there are deviations of about 3%, which provides an estimate of the numerical accuracy of the CSH cross sections in Tables 2 and 3.

Simple propensity rules predict that  $j \rightarrow j' \approx j$  transitions should dominate for heavy + light-heavy atom reactions [7] and Tables 2 and 3 show this to be the case. However, the  $j \rightarrow j' \approx j$  propensity rule does not apply to the smaller cross sections. This point has been examined in detail in our earlier CSDW calculations for BCMR and PK3 – see in particular Fig. 1 of Ref. [12]. In general, PK3 obeys

Table 3

Degeneracy averaged integral cross sections  $Q_{vj \rightarrow v'j'}(E)$  at  $E = 0.70$  eV for the PK3 potential energy surface. The five largest cross sections with  $v = 0$  and the four largest cross sections with  $v = 1$  are reported. Also listed as the corresponding rovibrational eigenvalues  $E_{vj}$  of the isolated HCl molecule

Label	$v$	$j$	$E_{vj}$ (eV)	$v'$	$j'$	$E_{v'j'}$ (eV)	$Q_{vj \rightarrow v'j'}$ ( $a_0^2$ )
a	0	0	0.183	0	1	0.186	1.276
b	0	0	0.183	0	2	0.191	1.123
c	0	1	0.186	0	1	0.186	0.960
d	0	1	0.186	0	2	0.191	0.846
e	0	0	0.183	0	0	0.183	0.569
f	1	0	0.537	1	1	0.540	1.903
g	1	1	0.540	1	1	0.540	1.223
h	1	0	0.537	1	2	0.545	1.166
i	1	0	0.537	1	0	0.537	1.024

Table 4

CSH and QCT degeneracy averaged integral cross sections  $Q_{vj}(E)$  at  $E = 0.70$  eV for the BCMR potential energy surface. The numbers in parentheses are powers of 10 by which the whole entry must be multiplied. The errors in the QCT cross sections correspond to  $\pm 1$  standard deviation

$v$	$j$	$Q_{vj}(a_0^2)$	
		CSH	QCT
0	0	0.97 (–1)	$0.29 \pm 0.05$ (–1) <sup>a</sup>
0	1	0.67 (–1)	
0	2	0.92 (–1)	$0.68 \pm 1.4$ (–1)
0	3	0.14	
0	4	0.20	$0.15 \pm 0.04$
0	5	0.28	
0	6	0.40	
0	7	0.48	
0	8	0.52	$0.50 \pm 0.07$
0	9	0.50	
0	10	0.45	
0	11	0.48	
0	12	0.78	$1.75 \pm 0.14$
0	13	0.82	$2.32 \pm 0.18$
0	14	0.86	$3.57 \pm 0.18$
0	15	0.75	$4.57 \pm 0.21$
0	16	0.61	$4.21 \pm 0.21$
0	17	0.20	$2.36 \pm 0.14$
0	18	0.70 (–2)	$< 0.46$ (–3)
0	19	0.68 (–5)	
1	0	0.62 (–1)	
1	1	0.86 (–1)	
1	2	0.14	
1	3	0.20	
1	4	0.28	
1	5	0.38	$0.30 \pm 0.01$ <sup>b</sup>
1	6	1.07	
1	7	0.60	
1	8	0.88 (–1)	
1	9	0.11 (–1)	
1	10	0.20 (–4)	

<sup>a</sup> QCT cross sections for  $v = 0$  are from Table 7 of Ref. [9].

<sup>b</sup> From Table I of Ref. [21].

simple propensity rules more closely than does BCMR.

We have also used the data in Figs. 1 and 2 to calculate at  $E = 0.70$  eV degeneracy-averaged integral cross sections summed over final states

$$Q_{vj}(E) = \sum_{v'} \sum_{j'} Q_{vj \rightarrow v'j'}(E),$$

where the sums are over all open states at the energy  $E$ . These cross sections are reported in Tables 4 and

Table 5

CSH and QCT degeneracy averaged integral cross sections  $Q_{vj}(E)$  at  $E = 0.70$  eV for the PK3 potential energy surface. The numbers in parentheses are powers of 10 by which the entry must be multiplied. The errors in the QCT cross sections correspond to  $\pm 1$  standard deviation

$v$	$j$	$Q_{vj}(\text{a}_0^2)$	
		CSH	QCT
0	0	4.17	$3.1 \pm 0.2^a$
0	1	3.20	$3.0 \pm 0.2$
0	2	1.82	$2.6 \pm 0.2$
0	3	0.80	$2.5 \pm 0.2$
0	4	0.45	$1.6 \pm 0.1$
0	5	0.44	$1.4 \pm 0.1$
0	6	0.45	$1.2 \pm 0.1$
0	7	0.37	$1.1 \pm 0.1$
0	8	0.31	$1.1 \pm 0.1$
0	9	0.27	$1.1 \pm 0.1$
0	10	0.22	$0.82 \pm 0.07$
0	11	0.17	$0.96 \pm 0.07$
0	12	0.14	$0.57 \pm 0.07$
0	13	0.75 (–1)	$0.39 \pm 0.04$
0	14	0.36 (–1)	$0.10 \pm 0.01$
0	15	0.65 (–2)	$< 0.1$ (–3)
0	16	0.20 (–3)	
0	17	0.55 (–5)	
0	18	0.46 (–7)	
0	19	0.11 (–9)	
1	0	5.62	
1	1	3.57	
1	2	1.32	
1	3	0.30	$0.19 \pm 0.01^b$
1	4	0.54 (–1)	
1	5	0.22 (–1)	
1	6	0.16 (–1)	
1	7	0.93 (–2)	
1	8	0.26 (–2)	
1	9	0.55 (–4)	
1	10	0.20 (–6)	

<sup>a</sup> QCT cross sections for  $v = 0$  are from Table 2 of Ref. [11].

<sup>b</sup> From Table I of Ref. [29] after applying linear interpolation to the cross sections at  $E_{\text{trans}}^{(v,j)} = 0.14$  and  $0.15$  eV, together with  $E = E_{\text{trans}}^{(v,j)} + E_{vj}$  where  $E_{vj} = 0.552$  eV for  $v = 1, j = 3$ . Note (i)  $E_{\text{trans}}^{(v,j)}$  is called  $E_{\text{col}}$  in Table I of Ref. [29], and (ii) the cross sections have units of  $\text{\AA}^2$ .

5, where they are compared with available QCT results [9,11,21,29].

For BCMR, the cross section ratio CSH/QCT varies from 0.08 to 3.3 whereas for PK3 the range is smaller, 0.18 to 1.5. Note for BCMR, the ratio is systematically  $> 1$  for states with small QCT cross sections, which may reflect tunnelling effects, and

systematically  $< 1$  for states which have large QCT cross sections. On PK3, the ratio is mostly  $< 1$ .

There are several possible reasons for these variations. The basis set used in the CSH( $\Omega = 0$ ) calculations may not be large enough to produce fully converged results at  $E = 0.70$  eV. Probably more important is the neglect of states with  $|\Omega| > 0$  in our CSH( $\Omega = 0$ ) computations. This point has been partially investigated in Ref. [23], where we compared CSH( $\Omega = 0$ ) cross sections (and other data) with the corresponding CCH( $\Omega_{\text{max}} = 2$ ) results for BCMR in the energy range  $E = 0.40$  (0.05) 0.60 eV. We found that agreement between the CSH( $\Omega = 0$ ) and CCH( $\Omega_{\text{max}} = 2$ ) results deteriorates as  $E$  increases, especially for states with large QCT cross sections. In particular, at  $E = 0.60$  eV,  $Q_{vj}(E)$  for  $v = 0, j = 12$  is larger by a factor of 2.7 for CCH( $\Omega_{\text{max}} = 2$ ) compared to CSH( $\Omega = 0$ ) – see Table 2 of Ref. [23]. The PK3 surface is more collinearly dominant than BCMR and so states with  $|\Omega| > 0$  should contribute less. This is consistent with the closer agreement between the CSH( $\Omega = 0$ ) and QCT cross sections in Table 5 compared to Table 4.

## 5. Reaction probabilities for $J = 0$

The energy dependence of the reaction probability for zero total angular momentum quantum number,  $P_{vj \rightarrow v'j'}^{J=0}(E)$ , is important for understanding the photo-detachment spectrum of  $\text{ClHCl}^-$  [17,18,35]. We consider its properties, and those of some related probabilities, in this Section for the nine transitions a, b, ..., i listed in Tables 2 and 3 for BCMR and PK3, respectively.

Fig. 3(a) displays  $P_{vj \rightarrow v'j'}^{J=0}(E)$  versus  $E$  for the nine transitions for BCMR, whilst Fig. 4(a) shows the corresponding plots for PK3.

We consider first transitions with  $v = 0 \rightarrow v' = 0$ . For both BCMR and PK3, the  $E$  dependence of the  $P_{0j \rightarrow 0j'}^{J=0}(E)$  is similar, with a rapid increase followed by a decline, thereby resulting in a broad peak (or reactivity oscillation). The peaks on PK3 have a similar shape which are centered around  $E \approx 0.45$  eV. In contrast, the peaks for BCMR are not aligned; rather they are shifted by approximately the difference in rotational energy of the  $\text{HCl}(v = 0, j)$  states – see Table 2.



To rationalise this behaviour, we invoke a simple hard-sphere model which exploits the different dynamics of the heavy and light atoms in the Cl + HCl reaction. This model assumes the motion of the heavy Cl atoms is unperturbed by the presence of the light H atom. In particular, the Cl atoms are brought together by their translational motion, followed by transfer of the H atom. This simple classical model suggests that translational energy

$$E_{\text{trans}}^{(v,j)} = E - E_{v,j}$$

should be an important variable for understanding the dynamics of the reaction.

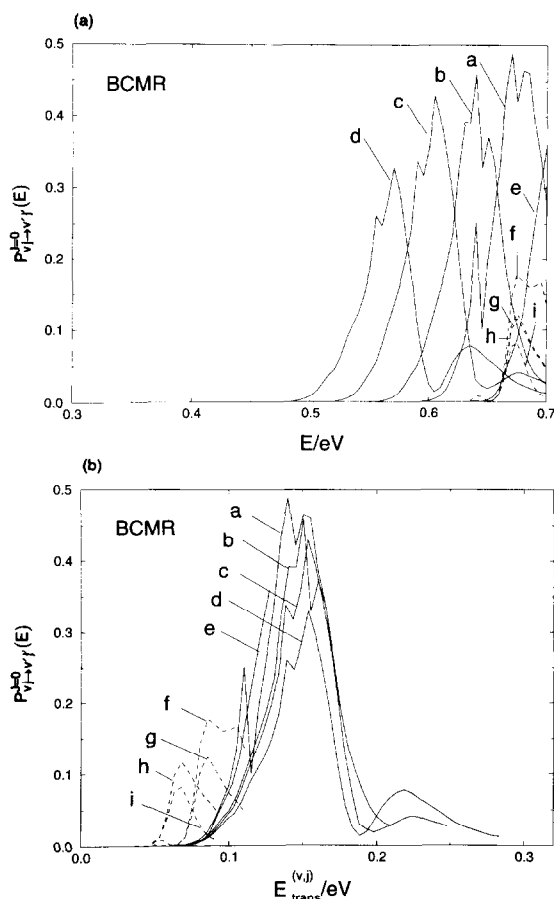


Fig. 3. (a) Plot of reaction probability  $P_{v_j \rightarrow v'f}^{J=0}(E)$  versus total energy  $E$  for the BCMR potential surface for the nine transitions a,b,...,i listed in Table 2. Solid lines represent transitions with  $v=0$  and dashed lines transitions with  $v=1$ . (b) Same as (a) except that translational energy  $E_{\text{trans}}^{(v,j)} = E - E_{v,j}$  is plotted along the abscissa. The rovibrational eigenvalues  $E_{v,j}$  of the isolated HCl( $v,j$ ) molecule are given in Table 2.

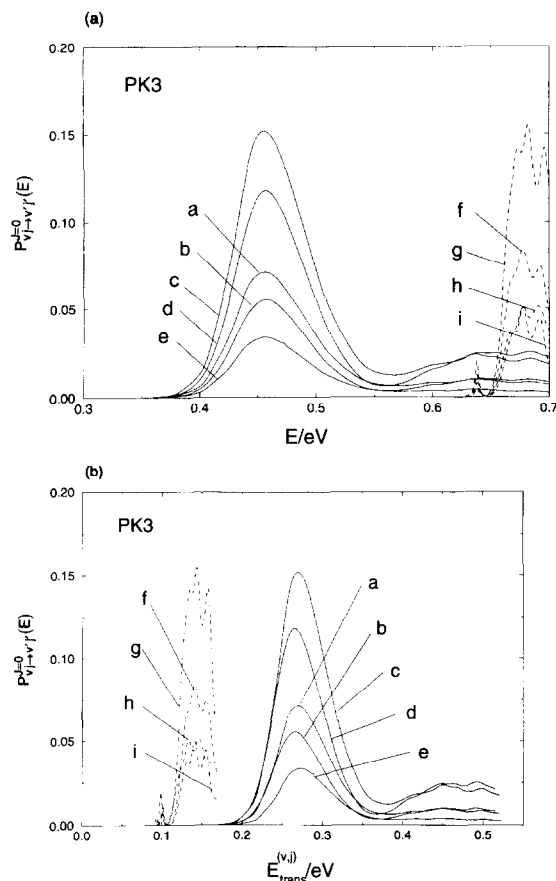


Fig. 4. (a) Plot of reaction probability  $P_{v_j \rightarrow v'f}^{J=0}(E)$  versus total energy  $E$  for the PK3 potential surface for the nine transitions a,b,...,i listed in Table 3. Solid lines represent transitions with  $v=0$  and dashed lines transitions with  $v=1$ . (b) Same as (a) except that translational energy  $E_{\text{trans}}^{(v,j)} = E - E_{v,j}$  is plotted along the abscissa. The rovibrational eigenvalues  $E_{v,j}$  of the isolated HCl( $v,j$ ) molecule are given in Table 3.

Fig. 3(b) and Fig. 4(b) show the state-to-state  $J=0$  reaction probabilities plotted against  $E_{\text{trans}}^{(v,j)}$  for BCMR and PK3, respectively. It can be seen for BCMR that the transitions with  $v=0 \rightarrow v'=0$  (i.e. a,b,c,d,e) have peaks which are now approximately centered around  $E_{\text{trans}}^{(v=0,j)} \approx 0.15$  eV. The corresponding transitions for PK3 in Fig. 4(b) are also aligned but in this case the effect of using  $E_{\text{trans}}^{(v,j)}$  rather than  $E$  on their alignment is small, because for example the difference  $E_{01} - E_{00}$  is only 0.003 eV.

Note for both surfaces, the reaction thresholds are considerably higher than the energy at which each

channel opens,  $E_{\text{trans}}^{(v=0,j)} = 0$ ; this helps justify the use of classical concepts. However, it is clear that the classical model will become invalid when rotation of the long-lived ClHCl complex is important, i.e. at the  $E = 0.642$  eV resonance on BCMR. Extensions to the model are described in Ref. [26].

Figs. 3 and 4 also display  $J = 0$  transitions which have  $v = 1 \rightarrow v' = 1$  (i.e. f,g,h,i). For both BCMR and PK3, the  $P_{1j \rightarrow 1j'}^{J=0}(E)$  show a steep rise at  $E \approx 0.65$  eV. As a result, for BCMR the reaction probabilities become more separated when plotted against  $E_{\text{trans}}^{(v=1,j)}$  – see Fig. 3(b) – whereas the PK3 results in Fig. 4(b) remain aligned. Evidently the separability assumption for the H and Cl motions is less valid for BCMR when the reactant HCl( $v,j$ ) molecule is vibrationally excited from  $v = 0$  to  $v = 1$ .

Fig. 5(a) and Fig. 5(b) show for BCMR and PK3, respectively, the  $J = 0$  vibrationally resolved reaction probability

$$P_{v \rightarrow v'}^{J=0}(E) = \sum_j \sum_{j'} P_{vj \rightarrow v'j'}^{J=0}(E),$$

and the  $J = 0$  cumulative reaction probability

$$\begin{aligned} P_{\text{cum}}^{J=0}(E) &= \sum_v \sum_{v'} P_{v \rightarrow v'}^{J=0}(E) \\ &= \sum_v \sum_{v'} \sum_j \sum_{j'} P_{vj \rightarrow v'j'}^{J=0}(E), \end{aligned}$$

both plotted against  $E$ . The sums are over all open states at the energy  $E$ . Note also that  $P_{0 \rightarrow 1}^{J=0}(E) \equiv P_{1 \rightarrow 0}^{J=0}(E)$ .

Both surfaces have an initial monotonic rise in  $P_{\text{cum}}^{J=0}(E)$  to approximately unity at  $E \approx 0.45$  eV, but then their behaviour is different. On BCMR,  $P_{\text{cum}}^{J=0}(E)$  has a shoulder followed by an irregular increase, whereas on PK3,  $P_{\text{cum}}^{J=0}(E)$  decreases before increasing again, which creates a reactivity oscillation. This different behaviour arises because, as explained above, on PK3 the peaks in  $P_{0j \rightarrow 0j'}^{J=0}(E)$  are aligned, whereas on BCMR they are displaced. The resonances at  $E = 0.638$  eV for PK3 and at  $E = 0.642$  eV for BCMR are clearly visible in the plots.  $P_{\text{cum}}^{J=0}(E)$  then has another smooth-step increase of approximately unity at  $E \approx 0.65$  eV for both surfaces, where transitions involving  $v = 1$  and  $v' = 1$  become important (see also Ref. [36]). It is important to emphasise that on PK3 the two peaks in  $P_{\text{cum}}^{J=0}(E)$  arise from two different mechanisms: the

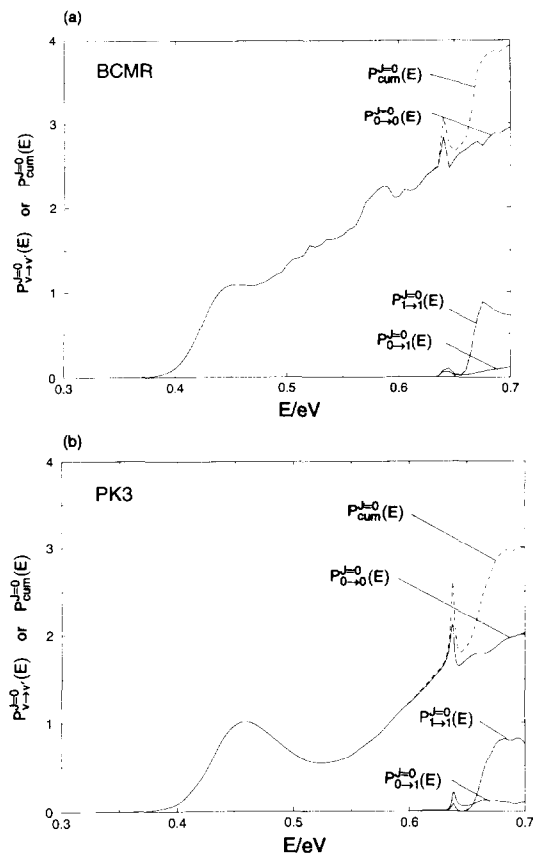


Fig. 5. (a) Plot of the reaction probability summed over initial and final rotational states  $P_{v \rightarrow v'}^{J=0}(E)$  versus  $E$  for the BCMR potential surface. Plots are shown for the transitions  $v = 0 \rightarrow v' = 0$ ,  $v = 0 \rightarrow v' = 1$  and  $v = 1 \rightarrow v' = 1$ . Note that  $P_{1 \rightarrow 0}^{J=0}(E) \equiv P_{0 \rightarrow 1}^{J=0}(E)$ . Also shown, as a dashed line, is the cumulative reaction probability,  $P_{\text{cum}}^{J=0}(E)$ . (b) Same as (a) except for the PK3 potential surface.

one at lower  $E$  is a reactivity oscillation, whilst the second one is a resonance.

## 6. Reactive angular distributions

### 6.1. Introduction

In this Section, we report reactive angular distributions for the BCMR and PK3 potential surfaces. The state-to-state differential cross sections in the CSH( $\Omega = 0$ ) approximation at an energy  $E$  are given by

$$\sigma_{vj \rightarrow v'j'}(\theta_R) = |f_{vj \rightarrow v'j'}(\theta_R)|^2,$$

where the scattering amplitude is

$$f_{vj \rightarrow v'j'}(\theta_R) = (2ik_{vj})^{-1} \sum_{J=0}^{\infty} (2J+1) S_{vj \rightarrow v'j'}^J(E) \times P_J(\cos(\pi - \theta_R)). \quad (6.1)$$

In these equations,  $P_J(\cdot)$  is a Legendre polynomial of degree  $J$  and  $\theta_R$  in the reactive scattering angle, i.e. the angle between the directions of the outgoing product HCl molecule and the incoming Cl atom. In addition, we have calculated angular distributions summed over final states

$$\sigma_{vj}(\theta_R) = \sum_{v'} \sum_{j'} \sigma_{vj \rightarrow v'j'}(\theta_R).$$

In order to understand structure in the differential cross sections, it is first helpful to examine the  $J$  dependence of the reaction probabilities  $P_{vj \rightarrow v'j'}^J(E)$ .

## 6.2. Dependence of reaction probabilities on $J$

Fig. 6(a) and Fig. 7(a) show, for the nine transitions in Table 2 (BCMR) and Table 3 (PK3), respectively, graphs of  $P_{vj \rightarrow v'j'}^J(E)$  versus  $J$  at  $E = 0.70$  eV. Comparing these graphs with those in Fig. 3(a) and Fig. 4(a) reveals that the  $P_{vj \rightarrow v'j'}^J(E)$  versus  $J$  plots are distorted mirror images of the  $P_{vj \rightarrow v'j'}^{J=0}(E)$  versus  $E$  ones.

This observation can be understood using the  $J$  shift approximation, which states

$$P_{vj \rightarrow v'j'}^J(E) \approx P_{vj \rightarrow v'j'}^{J=0}(E - B^\ddagger J(J+1)), \quad (6.2)$$

$J = 0, 1, 2, \dots,$

where  $B^\ddagger$  is the rigid rotator constant for  $\text{ClHCl}^\ddagger$  at the transition state. The  $J$  shift approximation assumes that increasing  $J$  is equivalent to reducing  $E$  by the rotational energy of the  $\text{ClHCl}^\ddagger$  complex. The approximation (6.2) predicts that the shape of a  $P_{vj \rightarrow v'j'}^J(E)$  versus  $J$  plot (at a fixed  $E$ ) is approximately the mirror image of the plot  $P_{vj \rightarrow v'j'}^{J=0}(E')$  versus  $E'$  for  $E' \leq E$ . However, the correspondence is expected to be distorted somewhat because the transformation in Eq. (6.2) is non-linear (quadratic) in  $J$ . It is clear that the  $J$  shift approximation accounts for the qualitative (mirror image) similari-

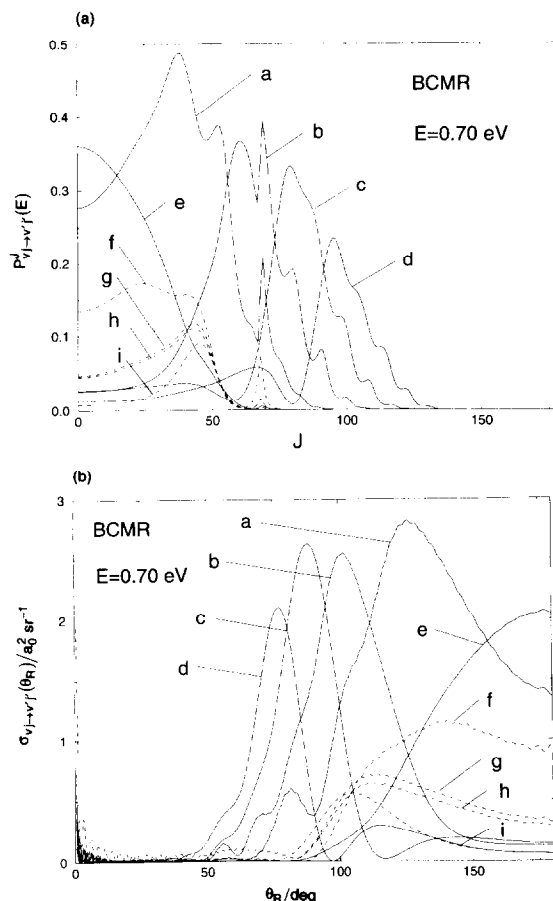


Fig. 6. (a) Plot of the reaction probability  $P_{vj \rightarrow v'j'}^J(E)$  versus  $J$  for the BCMR potential surface at  $E = 0.70$  eV for the nine transitions a,b,...,i listed in Table 2. Solid lines represent transitions with  $v = 0$  and dashed lines transitions with  $v = 1$ . (b) State-to-state differential cross section  $\sigma_{vj \rightarrow v'j'}(\theta_R)$  versus  $\theta_R$  for the BCMR potential surface at  $E = 0.70$  eV for the same nine transitions as in (a).

ties between Fig. 3(a) and Fig. 6(a) for BCMR and between 4(a) and 7(a) for PK3.

Note that Fig. 6(a) and Fig. 7(a) show transitions with  $v = 0 \rightarrow v' = 0$  occur for PK3 at larger total angular momentum quantum numbers,  $J \approx 130$ , than for BCMR, which receives its main contribution from lower values of  $J$  in the range 0–100. This is also consistent with the  $J$  shift approximation, on noting that the main peaks for the  $P_{0j \rightarrow 0j'}^{J=0}(E)$  curves in Fig. 4(a) for PK3 occur at lower  $E$  values than those for BCMR in Fig. 3(a). Fig. 6(a) and Fig. 7(a) also show that the resonance for both surfaces occurs

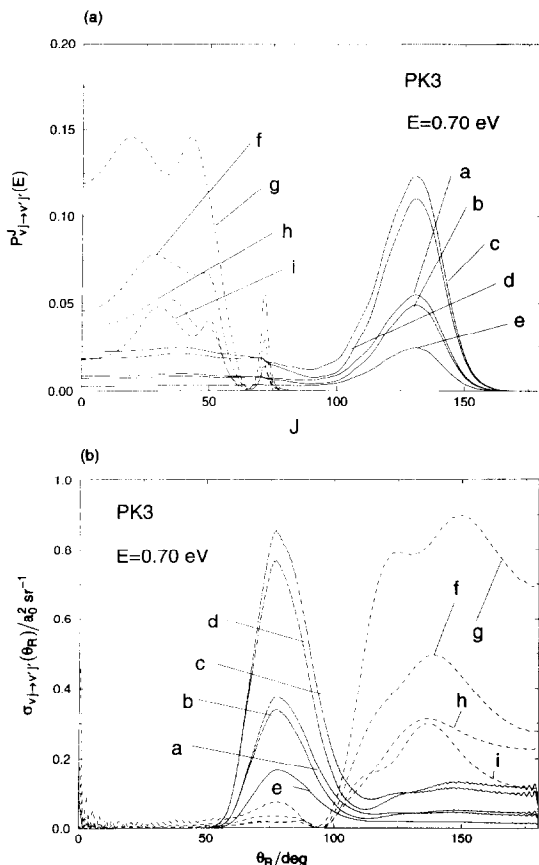


Fig. 7. (a) Plot of the reaction probability  $P_{vj \rightarrow v'f}^J(E)$  versus  $J$  for the PK3 potential surface at  $E = 0.70$  eV for the nine transitions a,b,...,i listed in Table 3. Solid lines represent transitions with  $v = 0$  and dashed lines transitions with  $v = 1$ . (b) State-to-state differential cross section  $\sigma_{vj \rightarrow v'f}(\theta_R)$  versus  $\theta_R$  for the PK3 potential surface at  $E = 0.70$  eV for the same nine transitions as in (a).

at  $J \approx 70$  for  $E = 0.70$  eV [n.b. although the  $v = 0 \rightarrow v' = 0$  transitions a,b,c,d,e for PK3 in Fig. 4(a) and Fig. 7(a) do not exhibit resonance behaviour, other  $v = 0 \rightarrow v' = 0$  transitions do show resonance structure, which creates the peak in  $P_{0 \rightarrow 0}^{J=0}(E)$  at  $E = 0.638$  eV in Fig. 5(b)].

### 6.3. State-to-state angular distributions

Fig. 6(b) and Fig. 7(b) display, for BCMR and PK3, respectively, the differential cross sections for the nine transitions. The scattering is largely confined to  $\theta_R \gtrsim 50^\circ$ , with PK3 showing more sideward

scattering for transitions with  $v = 0 \rightarrow v' = 0$ . In addition there are high frequency oscillations extending to forward angles. The oscillations are approximately in phase.

In order to understand the structure of the angular distributions, we use a semi-classical optical model, which is an extension of the simple classical model introduced in Section 5. The optical model makes the following assumptions when calculating differential cross sections.

(a) The scattering of the Cl atoms, which is not influenced by the H atom, is represented by the collision of two hard-spheres of radius  $r$ . The resulting angular distribution is isotropic,  $\sigma^{\text{hs}}(\theta_R) = r^2$ , with the relation between  $\theta_R$  and impact parameter  $b$  given by

$$\left. \begin{aligned} \theta_R &= 2 \cos^{-1}(b/(2r)), & b \leq 2r \\ &= 0, & b > 2r \end{aligned} \right\} \quad (6.3)$$

(b) The role of the H atom is to determine which impact parameters lead to reaction. If the classical reaction probability distribution function is denoted  $P_{vj \rightarrow v'f}(b)$  then the reactive differential cross section is given by

$$\left. \begin{aligned} \sigma_{vj \rightarrow v'f}^{\text{opt}}(\theta_R) &= r^2 P_{vj \rightarrow v'f}(b(\theta_R)), & b \leq 2r \\ &= 0, & b > 2r \end{aligned} \right\} \quad (6.4)$$

and Eq. (6.3) is also used.

In order to apply Eqs. (6.3) and (6.4) to the CSH scattering data, we must also make the identifications  $b \approx J/k_{vj}$

and

$$P_{vj \rightarrow v'f}(b) \approx P_{vj \rightarrow v'f}^J,$$

which means  $J = J(\theta_R) \propto \cos(\theta_R/2)$ , provided  $b \leq 2r$ . Note that larger  $J$ s lead to scattering into smaller angles.

These equations imply that the angular scattering is a distorted mirror image of the  $P_{vj \rightarrow v'f}^J(E)$  versus  $J$  plot, or equivalently a distorted version of the  $P_{vj \rightarrow v'f}^{J=0}(E')$  versus  $E'$  plot for  $E' \leq E$ . Comparison of Fig. 6(b) with Fig. 3(a) and Fig. 6(a) for BCMR, and comparison of Fig. 7(b) with Fig. 4(a) and Fig. 7(a) for PK3, show that this is indeed the case – with one important exception.

The exception concerns the resonance, which occurs at  $E \approx 0.64$  eV in Fig. 3(a) and Fig. 4(a) and at  $J \approx 70$  in Fig. 6(a) and Fig. 7(a). The sharp resonance peaks are not present in the  $\sigma_{v_j \rightarrow v'_j}(\theta_R)$  versus  $\theta_R$  plots. The explanation for this is that the semi-classical optical model assumes direct specular collision dynamics. This assumption breaks down for a resonance when a long-lived ClHCl complex is formed. Rotation and decay of the complex gives rise to an exponential tail stretching into the forward direction. In a semi-classical complex angular momentum (Regge pole) treatment, this forward angle scattering is accompanied by high frequency oscillations which arise from the interference of waves travelling around the target.

We have verified the physical interpretation just discussed in a different way by carrying out an asymptotic nearside–farside (NF) analysis of the angular scattering [22,33]. We did this by first making the asymptotic decomposition

$$P_J(\cos(\pi - \theta_R)) \sim P_J^N(\theta_R) + P_J^F(\theta_R), \quad (6.5)$$

where

$$P_J^{N,F}(\theta_R) = \left[ 2\pi \left( J + \frac{1}{2} \right) \sin \theta_R \right]^{-1/2} \times \exp \left\{ \pm i \left[ \left( J + \frac{1}{2} \right) (\pi - \theta_R) - \frac{1}{4} \pi \right] \right\}. \quad (6.6)$$

Eqs. (6.5) and (6.6) are just the asymptotic (large  $J$ ) approximation for  $P_J(\cos(\pi - \theta_R))$ . The term

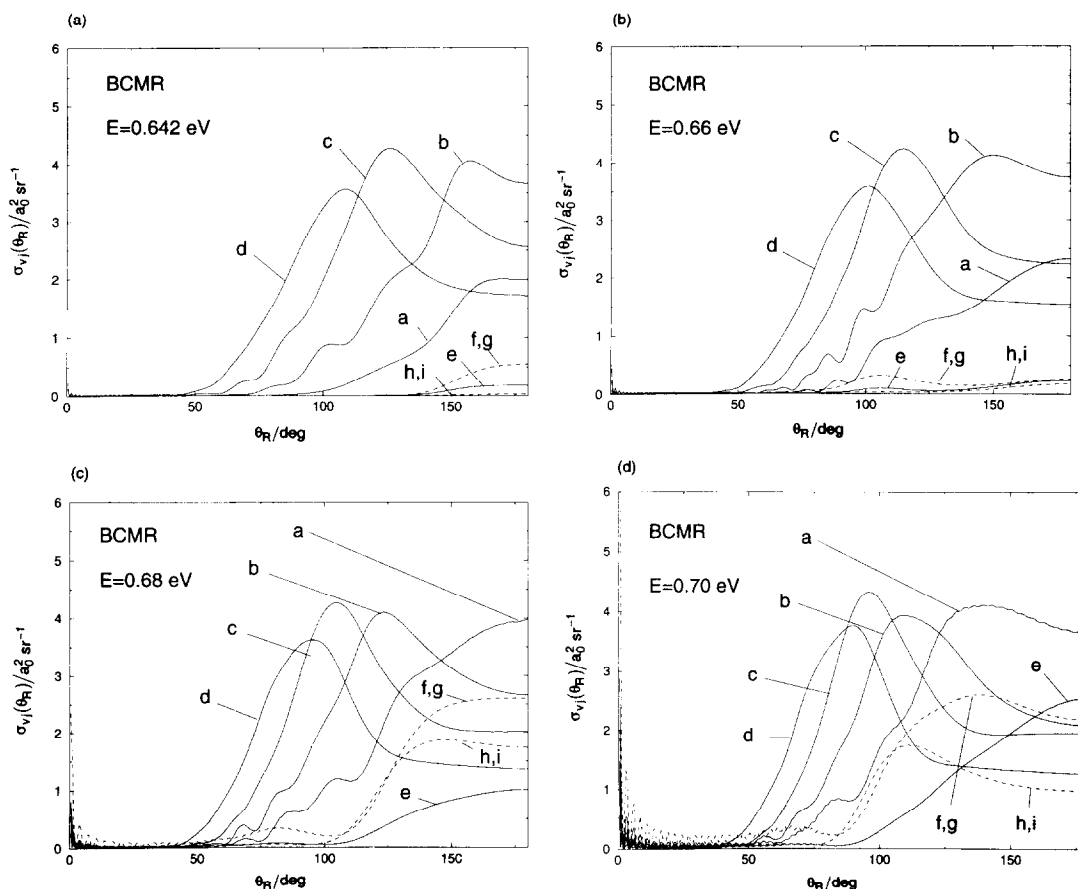


Fig. 8. Plot of differential cross section summed over final rovibrational states  $\sigma_{v_j}(\theta_R)$  versus  $\theta_R$  for the BCMR potential surface. The labels a.b....i listed in Table 2 are used to identify the initial rovibrational quantum numbers. Note that the pair f,g give identical results because they have the same values of  $v$  and  $j$ . This is also true for the pair h,i. (a)  $E = 0.642$  eV, (b)  $E = 0.66$  eV, (c)  $E = 0.68$  eV, (d)  $E = 0.70$  eV.

$P_j^N(\theta_R)$  corresponds physically to a travelling angular wave from the nearside of the target, and  $P_j^F(\theta_R)$  corresponds to a farside wave [22,33].

The scattering amplitude (6.1) can now be written in the form

$$f_{vj \rightarrow v'j'}(\theta_R) = f_{vj \rightarrow v'j'}^N(\theta_R) + f_{vj \rightarrow v'j'}^F(\theta_R), \quad (6.7)$$

where

$$f_{vj \rightarrow v'j'}^{N,F}(\theta_R) = (2ik_{vj})^{-1} \sum_{J=0}^{\infty} (2J+1) S_{vj \rightarrow v'j'}^J(E) P_j^{N,F}(\theta_R). \quad (6.8)$$

Structure in the angular distributions can arise from  $f_{vj \rightarrow v'j'}^N(\theta_R)$ , or from  $f_{vj \rightarrow v'j'}^F(\theta_R)$ , or from their interference  $f_{vj \rightarrow v'j'}^N(\theta_R) + f_{vj \rightarrow v'j'}^F(\theta_R)$ . It is important to note that Eqs. (6.5)–(6.8) use only the original CSH( $\Omega = 0$ ) scattering matrix elements  $S_{vj \rightarrow v'j'}^J(E)$ . Semi-classical procedures, such as stationary phase integration are not invoked, although the semi-classical picture is still evident.

We have applied this asymptotic  $NF$  theory to the angular distributions in Fig. 6(b) and Fig. 7(b). It shows that the forward-angle high frequency oscillations are a nearside–farside interference effect, whilst the structures for  $\theta_R \geq 50^\circ$  are dominated by near-

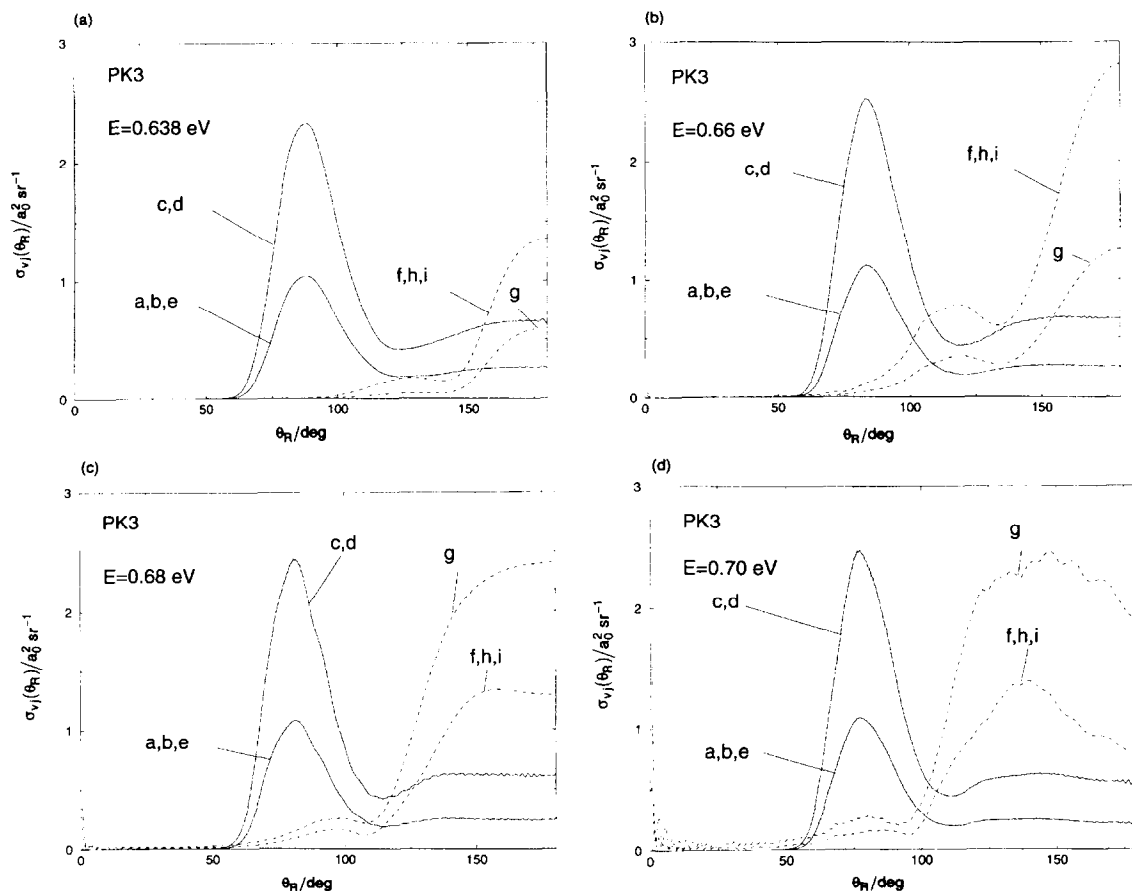


Fig. 9. Plot of differential cross section summed over final rovibrational states  $\sigma_{vj}(\theta_R)$  versus  $\theta_R$  for the PK3 potential surface. The labels a, b, ..., i listed in Table 3 are used to identify the initial rovibrational quantum numbers. Note that the pair c, d give identical results because they have the same values of  $v$  and  $j$ . This is also true for the triples a, b, e and f, h, i. (a)  $E = 0.638$  eV, (b)  $E = 0.66$  eV, (c)  $E = 0.68$  eV, (d)  $E = 0.70$  eV.

side scattering – see Ref. [22] for similar example. This *NF* interpretation of the scattering for  $\theta_R \geq 50^\circ$  is consistent with the semi-classical optical model (which cannot, however, properly describe the forward angle scattering).

#### 6.4. Angular distributions summed over final states

We have also calculated differential cross sections summed over final states  $\sigma_{vj}(\theta_R)$ . They are shown in Fig. 8 for BCMR at  $E = 0.642, 0.66, 0.68, 0.70$  eV and in Fig. 9 for PK3 at  $E = 0.638, 0.66, 0.68, 0.70$  eV. The values used for  $v, j$  are the same as those in Tables 2 and 3, i.e. the labels a, b, ..., i, in the figures now identify the initial rovibrational quantum numbers.

The  $\sigma_{vj}(\theta_R)$  at  $E = 0.70$  eV are similar in shape to the state-to-state angular distributions in Fig. 6(b) or Fig. 7(b) – this is expected since the  $\sigma_{vj \rightarrow v'j'}(\theta_R)$  in Fig. 6(b) and Fig. 7(b) provide the dominant contributions to the  $\sigma_{vj}(\theta_R)$ . As  $E$  increases, the scattering generally moves to forward angles – this effect is more pronounced for transitions with  $v = 1$ . Note also the forward-angle high-frequency oscillations are not quenched on summing over final states; this fact should help their experimental detection.

## 7. Conclusions

We have calculated, for the PK3 potential energy surface, CSH( $\Omega = 0$ ) state-to-state and cumulative reaction probabilities, and differential and integral cross sections. We systematically compared the PK3 results with corresponding ones from the BCMR potential surface.

BCMR is an example of a ‘loose-bend’ potential: HCl can rotate relatively freely all the way to, and from, the saddle point. In contrast, PK3 is a ‘tight-bend’ potential, in which the H atom exchange is constrained to a nearly collinear configuration of the atoms. Our CSH results are consistent with these classical concepts. In particular, at  $E = 0.70$  eV, the largest  $Q_{vj \rightarrow v'j'}(E)$  with  $v = v' = 0$  or 1 have high  $j, j'$  values for BCMR (Fig. 1 and Table 2), whereas rotationally cold reactants and products are preferred on PK3 (Fig. 2 and Table 3).

For both potentials, the non-resonance aspects of the reaction dynamics can be understood qualita-

tively with the help of three simple models. The hard-sphere model for the collision of the reactants assumes that the translational motion of the Cl atoms is unperturbed by the H atom motion. It implies that translational energy,  $E_{\text{trans}}^{(v,j)}$ , is an important dynamical variable, and this was found to be the case for the  $P_{vj \rightarrow v'j'}^{J=0}(E)$  curves which we studied (except for transitions with  $v = 1 \rightarrow v' = 1$  on BCMR) – see Fig. 3(b) and Fig. 4(b).

The cumulative probability  $P_{\text{cum}}^{J=0}(E)$  for both surfaces rises smoothly by about unity at total energies where transitions with  $v = 0$  and  $v = 1$  become important.  $P_{\text{cum}}^{J=0}(E)$  for PK3 possesses a reactivity oscillation, whereas on BCMR, it does not (Fig. 5(a) and Fig. 5(b)). This behaviour arises because on PK3 the peaks in  $P_{0j \rightarrow 0j'}^{J=0}(E)$  are aligned, whereas on BCMR they are displaced.

The  $J$  dependence of the  $P_{vj \rightarrow v'j'}^J(E)$ , at a fixed  $E$ , can be understood using the  $J$  shift approximation. A plot of  $P_{vj \rightarrow v'j'}^J(E)$  versus  $J$  is a distorted mirror image of the corresponding  $P_{vj \rightarrow v'j'}^{J=0}(E')$  versus  $E'$  plot for  $E' \leq E$ ; see Fig. 6(a) and Fig. 7(a).

The semi-classical optical model shows that the  $\sigma_{vj \rightarrow v'j'}(\theta_R)$  versus  $\theta_R$  plot, at a fixed  $E$ , is also a distorted mirror image of the corresponding  $P_{vj \rightarrow v'j'}^J(E)$  versus  $J$  plot, and thus is similar to the  $P_{vj \rightarrow v'j'}^{J=0}(E')$  versus  $E'$  plot for  $E' \leq E$  (Fig. 6(b) and Fig. 7(b)). An important exception to this rule concerns the resonance for both surfaces, which is transformed into forward-angle high frequency oscillations in the differential cross sections. An (asymptotic) *NF* analysis reveals that the oscillations arise from the interference of nearside and farside waves that propagate around the target. Figs. 6 and 9 show that these oscillations survive summation over final states, which should aid their experimental detection.

## Acknowledgements

The support of this research by the UK Engineering and Physical Sciences Research Council and the US Department of Energy, Office of Basic Energy Sciences under contract W-31-109-ENG-38 is gratefully acknowledged. The computations were carried out at the Manchester Computing Centre, UK and the National Center for Supercomputing Applications, USA.

## References

- [1] F.S. Klein, A. Persky and R.E. Weston Jr., *J. Chem. Phys.* 41 (1964) 1799; F.S. Klein and A. Persky, *J. Chem. Phys.* 59 (1973) 2775; B.C. Garrett, D.G. Truhlar, A.F. Wagner and T.H. Dunning Jr., *J. Chem. Phys.* 78 (1983) 4400.
- [2] M. Kneba and J. Wolfrum, *J. Phys. Chem.* 83 (1979) 69; *Ann. Rev. Phys. Chem.* 31 (1980) 47.
- [3] R.B. Metz, T. Kitsopoulos, A. Weaver and D.M. Neumark, *J. Chem. Phys.* 88 (1988) 1463; R.B. Metz, A. Weaver, S.E. Bradforth, T.N. Kitsopoulos and D.M. Neumark, *J. Phys. Chem.* 94 (1990) 1377.
- [4] D.K. Bondi, J.N.L. Connor, J. Manz and J. Römelt, *Mol. Phys.* 50 (1983) 467.
- [5] A.B. McCoy, R.B. Gerber and M.A. Ratner, *J. Chem. Phys.* 101 (1994) 1975; N. Rougeau and C. Kubach, *Chem. Phys. Letters* 228 (1994) 207; Z.-Q. Zhao, W.B. Chapman and D.J. Nesbitt, *J. Chem. Phys.* 102 (1995) 7046; G.C. Schatz, *J. Phys. Chem.* 99 (1995) 7522; A.B. McCoy, *J. Chem. Phys.* 103 (1995) 986; *Mol. Phys.* 85 (1995) 965; C. Leforestier, K. Yamashita and N. Moiseyev, *J. Chem. Phys.* 103 (1995) 8468.
- [6] A. Persky and H. Kornweitz, *J. Phys. Chem.* 91 (1987) 5496.
- [7] G.C. Schatz, B. Amaee and J.N.L. Connor, *Chem. Phys. Letters* 132 (1986) 1.
- [8] G.C. Schatz, B. Amaee and J.N.L. Connor, *Comput. Phys. Commun.* 47 (1987) 45.
- [9] B. Amaee, J.N.L. Connor, J.C. Whitehead, W. Jakubetz and G.C. Schatz, *Faraday Disc. Chem. Soc.* 84 (1987) 387.
- [10] G.C. Schatz, B. Amaee and J.N.L. Connor, *J. Phys. Chem.* 92 (1988) 3190.
- [11] J.N.L. Connor and W. Jakubetz, in: *Supercomputer algorithms for reactivity, dynamics and kinetics of small molecules*, Proc. NATO Adv. Res. Workshop, Colombella di Perugia, Italy, 30 August–3 September 1988, ed. A. Laganà (Kluwer, Dordrecht, 1989) p. 395.
- [12] G.C. Schatz, B. Amaee and J.N.L. Connor, *J. Chem. Phys.* 92 (1990) 4893.
- [13] G.C. Schatz, B. Amaee and J.N.L. Connor, *J. Chem. Phys.* 93 (1990) 5544.
- [14] G.C. Schatz, *Chem. Phys. Letters* 150 (1988) 92.
- [15] G.C. Schatz, *Chem. Phys. Letters* 151 (1988) 409.
- [16] Q. Sun, J.M. Bowman, G.C. Schatz, J.R. Sharp and J.N.L. Connor, *J. Chem. Phys.* 92 (1990) 1677.
- [17] G.C. Schatz, *J. Chem. Phys.* 90 (1989) 3582.
- [18] G.C. Schatz, *J. Phys. Chem.* 94 (1990) 6157.
- [19] G.C. Schatz, D. Sokolovski and J.N.L. Connor, *J. Chem. Phys.* 94 (1991) 4311.
- [20] G.C. Schatz, D. Sokolovski and J.N.L. Connor, *Faraday Disc. Chem. Soc.* 91 (1991) 17.
- [21] W. Jakubetz, D. Sokolovski, J.N.L. Connor and G.C. Schatz, *J. Chem. Phys.* 97 (1992) 6451.
- [22] J.N.L. Connor, P. McCabe, D. Sokolovski and G.C. Schatz, *Chem. Phys. Letters* 206 (1993) 119.
- [23] G.C. Schatz, D. Sokolovski and J.N.L. Connor, *Can. J. Chem.* 72 (1994) 903.
- [24] G.C. Schatz, D. Sokolovski and J.N.L. Connor, in: *Advances in molecular vibrations and collision dynamics*, ed. J.M. Bowman (JAI Press, Greenwich, 1994), Vol. 2B, p. 1.
- [25] D. Sokolovski, J.N.L. Connor and G.C. Schatz, *Chem. Phys. Letters* 238 (1995) 127.
- [26] D. Sokolovski, J.N.L. Connor and G.C. Schatz, *J. Chem. Phys.* 103 (1995) 5979.
- [27] A. Persky and H. Kornweitz, *Chem. Phys.* 130 (1989) 129; A. Persky and H. Kornweitz, *Chem. Phys. Letters* 159 (1989) 134; H. Kornweitz and A. Persky, *Chem. Phys.* 132 (1989) 153; H. Kornweitz, M. Broida and A. Persky, *J. Phys. Chem.* 93 (1989) 251; H. Kornweitz, A. Persky and R.D. Levine, *J. Phys. Chem.* 95 (1991) 1621.
- [28] J.P. Fulmer and P.M. Aker, *J. Chem. Phys.* 96 (1992) 4252.
- [29] P.M. Aker and J.P. Fulmer, *J. Chem. Phys.* 99 (1993) 244.
- [30] J.M. Bowman and A.F. Wagner, in: *The theory of chemical reaction dynamics*, Proc. NATO Adv. Res. Workshop, Orsay, France, 17–30 June 1985, ed. D.C. Clary (Reidel, Dordrecht, 1986) p. 47; J.M. Bowman, *Adv. Chem. Phys.* 61 (1985) 115; *J. Phys. Chem.* 95 (1991) 4960.
- [31] K. Takayanagi, *Prog. Theo. Phys.* 8 (1952) 497.
- [32] D.R. Herschbach, *Appl. Opt. Suppl.* no 2 (1965) 128; *Adv. Chem. Phys.* 10 (1966) 319.
- [33] P. McCabe and J.N.L. Connor, *J. Chem. Phys.* 104 (1996) 2297.
- [34] M.A. Vincent, J.N.L. Connor, M.S. Gordon and G.C. Schatz, *Chem. Phys. Letters* 203 (1993) 415; L. Visscher and K.G. Dyall, *Chem. Phys. Letters* 239 (1995) 181; Y. Bu, Z. Cao and X. Song, *Int. J. Quant. Chem.* 57 (1996) 95.
- [35] J.M. Bowman and B. Gazdy, *J. Phys. Chem.* 93 (1989) 5129; B. Gazdy and J.M. Bowman, *J. Chem. Phys.* 91 (1989) 4615; J.M. Bowman, B. Gazdy and Q. Sun, *J. Chem. Soc., Faraday Trans.* 86 (1990) 1737.
- [36] D.C. Chatfield, R.S. Friedman, G.C. Lynch and D.G. Truhlar, *Faraday Disc. Chem. Soc.* 91 (1991) 398; *J. Phys. Chem.* 96 (1992) 57.